Modelling of materials properties in duplex stainless steels

X. Li, A. P. Miodownik, and N. Saunders

Work is being undertaken to develop a new multiplatform software programme for predicting a wide range of materials properties for various alloy types. These properties include thermophysical and physical properties, mechanical properties, time–temperature transformation (TTT)/continuous cooling transformation diagrams etc. and the calculations are being applied to a variety of multicomponent alloy types, such as Ni based superalloys, steels, Ti alloys, Al alloys. The current paper concentrates on duplex stainless steels and describes the scientific background used for the calculation of TTT diagrams and mechanical properties for these materials. It is shown that there is very good agreement between the calculated TTT diagrams and the observed results from the literature for the formation of the σ, χ, and the chromium rich α' phase, while the calculated proof stress, tensile stress and hardness are in good agreement with the available experimental data. The effects of solution treatment temperature and the volume fraction of σ phase on mechanical properties are also discussed. **MST/5133**

The authors are with Thermotech Ltd, Surrey Technology Centre, Surrey Research Park, Guildford, Surrey GU2 7YG, UK (x.li@thermotech.co.uk). *Manuscript received 16 June 2001; 10 September 2001.*

Introduction

Duplex stainless steels (DSSs), which normally contain 22–25Cr, 2–4Mo, 4–7Ni, and 0·1–0·27N (wt-%) and approximately equal amounts of ferrite (α) and austenite (γ), have many applications owing to their excellent combination of mechanical strength, toughness, and corrosion resistance. (All compositions in this paper are given in wt-% unless otherwise stated.) The various grades of DSS are usually defined by the pitting resistant equivalent number (PREN), which can be expressed as[1]

$$\text{PREN} = [\text{Cr}] + 3{\cdot}3([\text{Mo}] + 0{\cdot}5[\text{W}]) + 16[\text{N}] \quad . \quad . \quad . \quad . \quad (1)$$

Duplex stainless steels can then be categorised as low alloyed (PREN: 24–25), medium alloyed (PREN: 29–35), high alloyed (PREN: 36–39), and super duplex (PREN > 40). Typical compositions of these grades are listed in Table 1.

Adding further Cr, Mo, W, and N could theoretically result in the development of alloys with improved pitting corrosion resistance. However, the level of addition is limited by the solubility of nitrogen in the matrix and by the fact that chromium, molybdenum and tungsten partition to the ferrite phase. This in turn promotes the formation of various types of precipitates,[2] for example, σ and χ form at higher exposure temperatures (550–1000°C), while α' forms in the temperature range 300–500°C, the so called '475°C' embrittlement.[3] The formation of these phases results in the depletion of alloying elements in solid solution, which is detrimental to toughness and corrosion resistance. Therefore, prior knowledge concerning the stability of the various precipitates and their kinetics of formation is highly desirable both for application to existing grades and for the design of new alloys. To this end, the ability to accurately model time–temperature transformation (TTT) diagrams represents an invaluable tool for the practical user of these alloys.

Additionally, it is well known that both the relative amounts of austenite and ferrite and their grain size will affect the mechanical properties of stainless steels. Most of the formulae developed so far to calculate mechanical properties have relied on regression analysis. In this case the input data is the composition of the alloy, volume fraction of the phases and their grain size.[4,5] This can be a time consuming procedure, usually reliant on experiment to provide data on volume fractions, with no guarantee that the desired combination of compositions and phases is realisable in practice. Recently, a new approach, which combines the results of CALPHAD predictions with calculation of mechanical properties, has been developed and applied to various multicomponent solid solutions.[6] This method starts with the prediction of the volume fraction and composition of the phases that result from a particular alloy composition and heat treatment, and simultaneously calculates selected mechanical properties in the same software package.

The present paper begins with a brief outline of the models used to calculate the TTT diagram and mechanical properties. This work is part of a more comprehensive computer programme, called JMatPro, developed to model materials properties for commercial multicomponent alloys.[7] The intention of the present work is to demonstrate the application of this approach to a wide range of DSSs, with the purpose of providing reliable models for the calculation of TTT diagrams and mechanical properties.

Description of model

THERMODYNAMIC CALCULATION OF PHASE EQUILIBRIA

One of the most critical factors in the successful modelling of materials properties is the ability to accurately calculate stable and metastable phase equilibria. The present work utilises what has become known as the CALPHAD method.[8]

Table 1 Typical chemical compositions of duplex stainless steels

Tradename	Standard (UNS S)	Composition, wt-% Cr	Mo	Ni	N	Other elements	PREN*
SAF 2304/UR 35N	32304	23	0·2	4	0·07	...	25
SAF 2205/UR 45N	31803	22	3	5·3	0·17	...	35
UR 52N	32550	25	3	6·5	0·18	1·6Cu	38
SAF 2507/UR52+	32750	25	3·8	7	0·27	...	42
ZERON 100	32760	25	3·6	7	0·25	0·7Cu, 0·7W	41

*PREN pitting resistant equivalent number.

The roots of the approach lie in the mathematical description of the thermodynamic properties of the phases of interest. Once the thermodynamics of the various phases are defined, phase equilibria can be calculated using Gibbs energy minimisation.[9] The current work uses the thermodynamic calculation facility EQLib, described in a previous paper.[7]

CALCULATION OF TIME–TEMPERATURE TRANSFORMATION DIAGRAMS

The evolution of the volume fraction x of a product phase during solid state transformation can be described using the classical Johnson–Mehl–Avrami equation,[10,11] which, for spherical particles and isothermal conditions, can be expressed as

$$x=\frac{V}{V_{eq}(T)}=1-\exp\left(-\frac{\pi}{3}N_r G_r^3 t^4\right) \quad . . . . . (2)$$

where T is the temperature, V is the volume fraction transformed at time t, V_{eq} is the equilibrium amount of precipitate, N_r is the nucleation rate, and G_r is the growth rate. A more general representation takes the form

$$x=1-\exp(-Kt^n) \quad . . . . . (3)$$

where K is a constant, subsuming effects associated with nucleation and growth, and usually empirically evaluated for each temperature, and n is the time exponent, often referred to as the Avrami exponent. In order for equation (3) to be applied successfully, it has long been known that n can vary in the range 1–4. Often, the various values of n are linked to factors such as shape, whether the nucleation or growth rate is constant or whether nucleant site saturation has been achieved. The effect of shape can be demonstrated by considering the growth of a disk when equation (3) becomes

$$x=1-\exp\left(-\frac{\pi}{3}N_r l_o G_r^2 t^3\right) \quad . . . . . (4)$$

where l_o is the constant thickness of the plate. If there is site saturation of nucleation sites, the equation for disks becomes

$$x=1-\exp(-\pi N_o l_o G_r^2 t^2) \quad . . . . . (5)$$

where N_o is the total number of active nucleant sites. It can be seen that these conditions reduce the power to which t needs to be raised. An extreme case would be for growth of a cylindrical needle combined with nucleation site saturation, in this case

$$x=1-\exp[-\pi(d_o/2)^2 N_o G_r t] \quad . . . . . (6)$$

where d_o is the constant diameter of the needle. In these simple cases, the Avrami exponent takes integer values of between 1 and 4. However, it is well known that a wide variety of non-integer values are needed to take into account the modelling of real materials such as those studied in this paper. This may be due to complex morphologies or non-linear growth rates or the fact that growth occurs by, for example, both plates and needles. In the latter case, growth is dependent on a combination of one- and two-dimensional morphologies. Whichever is the case, if non-integer values are used for the Avrami exponent, the relevant equation must be formulated in such a way that dimensionality is maintained. To this end, the following approximations have been proposed to take into account the effect of shape.[12] For conditions where steady state nucleation operates

$$x=1-\exp\left(-f\frac{l_c^{3-p}}{p+1}N_r G_r^p t^{p+1}\right) \quad . . . . . (7)$$

While for the case where nucleant site saturation has been reached, the proposed relation is

$$x=1-\exp(-f l_c^{3-p} N_o G_r^p t^p) \quad . . . . . (8)$$

where f is a shape factor,[11] and l_c is a 'critical dimension', equivalent to l_o or d_o in equations (4)–(6). For σ and χ, a value for l_c of 50 nm is assumed to be reasonable, and for the case of α', which forms as very thin disks, l_c is taken as 2·5 nm. Based on equations (2)–(6) values for f will vary between 1 and 4. However, it has been found that such a variation actually makes relatively small changes to the final calculations and, in the present case, a value of unity has been assumed.

For the successful calculation of TTT diagrams, the above equations rely on the ability to calculate both nucleation and growth rates. In the present work, the nucleation rate N_r was obtained by modifying the previous equations used by Saunders and Miodownik[13] for nucleation from the liquid to include an effective wetting angle

$$N_r=\frac{N_o D_{eff}}{a_o^2}\exp\left(-\frac{G^*}{kT}\right)$$
$$=\frac{N_o D_{eff}}{a_o^2}\exp\left[-\frac{16\pi\alpha^3}{3NkT}f(\theta)\frac{\Delta H_m^3}{\Delta G_m^2}\right] \quad . . . . (9)$$

where N_o is the number of potential sites for nucleation, a_o is an atomic spacing, G^* is the Gibbs energy barrier to nucleation, k is Boltzman's constant, N is Avagadro's number, T is the temperature, α is a constant relating ΔH_m to the matrix/nucleus interfacial energy, θ is a wetting angle, $f(\theta)=(2-3\cos\theta+\cos^3\theta)/4$, and ΔH_m and ΔG_m are the enthalpy and molar Gibbs energy driving force of transformation respectively.

The original derivation of G^* assumed that the matrix/nucleus interfacial energy is related to ΔH_m via a constant α and that the surface energy is isotropic in nature,[14] which is unlikely to be the general case in the solid state. Nevertheless, it is considered that the enthalpy of transformation does play a part in the chemical Gibbs energy part of the surface energy and this potentially allows this parameter to be considered in a comparative and systematic fashion. The value of the wetting angle is found empirically. It is taken to represent the efficacy of a heterogeneous nucleation site and, therefore, subsumes effects associated with the anisotropic nature of the surface energy. In many of the cases considered so far, it has been found that θ is small and nucleation so easy that conditions of nucleant site saturation apply.[12]

The diffusion coefficient D_{eff} in the above equation is taken as concentration dependent and calculated using the following expressions

$$D_{eff}=D_o^\alpha\exp(-Q_{eff}/RT) \quad . . . . . (10)$$

where

$$D_o^\alpha=\sum_i x_i D_i^0 \quad . . . . . (11)$$

and

$$Q_{eff}=\sum_i x_i Q_i \quad . . . . . (12)$$

In equations (11) and (12), x_i is the mole fraction of element i in the precipitate and D_i^0 and Q_i are the frequency factor and activation energy for the diffusion of element i in the ferrite matrix. Following experimental observation, the precipitation of the various phases of interest (here, σ, χ, and α') is taken to occur from the ferrite phase that is formed at the duplexing temperature and the requisite values of D_i^0 and Q_i are taken from literature.[15,16]

The growth rate of a precipitate can be calculated using the following equation[11]

$$G_r=\mu\Delta G \quad . . . . . (13)$$

where μ is the interface mobility and combines factors such as diffusivity (in this case calculated by equations (10)–(12)) and the atomic vibration frequency. The driving force

for growth in atomic units is ΔG and is directly calculated from ΔG_m. Explicitly inputting the diffusivity and molar driving force into equation (13) gives

$$G_r = \kappa D_{eff} \left(\frac{\Delta G_m}{RT} \right) \quad \ldots \ldots \ldots \ldots \quad (14)$$

where κ is a constant. In the present work κ has been empirically evaluated and its value tested against theoretical estimates where agreement is very good. Except for a true invariant reaction, such as a eutectoid transformation, an important feature is that ΔG_m can vary as a function of amount transformed. For example, as growth of a precipitate from a supersaturated solid solution proceeds to equilibrium, ΔG_m can vary between a maximum at the beginning of transformation and zero on completion. This creates complications in solving the basic equations. However, where the amount of transformation remains relatively small, as for the present calculations, the value of ΔG_m at the start of transformation may provide a reasonable approximation. If ΔG_m varies sharply, or more substantial fractions transformed need to be calculated, the decrease in growth rate as a function of x needs to be considered and this will be discussed in a further paper.[12]

In order to perform the TTT diagram calculations, the first step is to build up a self-consistent diffusion database for D_i^0 and Q_i and obtain values of x_i, ΔH_m, and ΔG_m via thermodynamic calculations. Apart from these terms, specific parameters for θ, N_0, and p were evaluated for the various precipitates mainly based on matching the experimental results for transformation in SAF 2205[17] and SAF 2507.[2,18]

CALCULATION OF MECHANICAL PROPERTIES

The yield or proof stress of single phase materials can be calculated using the standard Hall–Petch equation[19]

$$\sigma_y = \sigma_o + k d^{-1/2} \quad \ldots \ldots \ldots \ldots \quad (15)$$

Where σ_y is the yield or proof stress, σ_o is the intrinsic flow stress, k is the Hall–Petch coefficient, and d is the grain size. Two types of databases for solid solution hardening have been created: one for flow stress and the other for Hall–Petch coefficients. These databases are similar in format to thermodynamic ones in that they comprise input coefficients for the pure metals and solid solution strengthening coefficients as a function of pairwise mixing of the various elements. It has been reported previously[6] that this approach can give a very good result for the solution hardened 0·2% proof stress in austenitic stainless steels and ferritic stainless steels. For DSS, the total proof stress can be obtained by the classical linear laws of mixtures, which is a special case of a more generalised approach[20]

$$\sigma_y = \sigma_y^{fcc} V_{fcc} + \sigma_y^{bcc} V_{bcc} \quad \ldots \ldots \ldots \ldots \quad (16)$$

where σ_y^{fcc} and σ_y^{bcc} are the proof stress for the austenite and ferrite phase respectively and V_{fcc} and V_{bcc} are the volume fraction of the two phases predicted by thermodynamic calculation at the solution heat treatment temperature.

Once the proof stress of DSS has been calculated, the ultimate tensile stress (UTS) and hardness can be derived from the inter-relationship between the proof stress, hardness and UTS as described previously.[6]

Results and discussion

PHASE EQUILIBRIA

Figure 1 shows the equilibrium phases present in a SAF 2205 alloy as a function of temperature. Validation

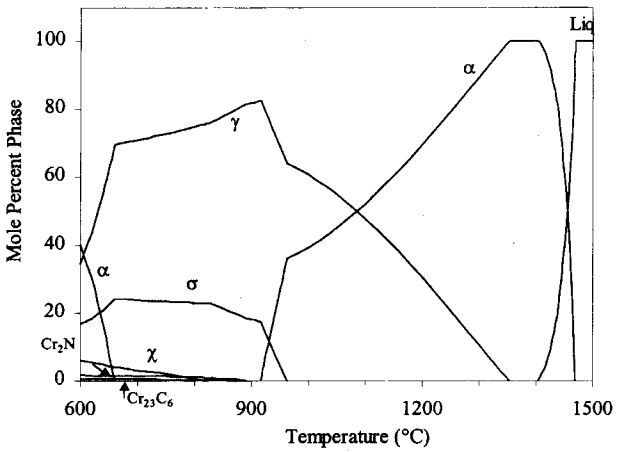

1 Calculated phase amount *v.* temperature plots for SAF 2205 alloy

of the calculated result against experiment shows that excellent agreement with known phase equilibria is found.[8] The change in the amounts of austenite and ferrite is calculated very well, the formation of σ and χ is correctly predicted while the formation of the $M_{23}C_6$ and Cr_2N also agrees well with experiment. Figure 1 can be taken to represent the general behaviour of most DSSs; the various temperature ranges of phase formation may change but, otherwise, the phases formed are very similar in most alloys of this type.

TIME–TEMPERATURE TRANSFORMATION DIAGRAMS

Time–temperature transformation diagrams for the precipitate in DSSs have been calculated as described in the previous section. When Si, Mn, and C are not mentioned in the original paper, a content of 0·4Si, 1Mn, and 0·01C has been assumed. Figure 2 shows the calculated TTT curves for the start of transformation (taken here as 0·5 vol.-% transformed) for σ and χ in a medium alloyed DSS SAF 2205 and compares these with the experimental results from Thorvaldsson.[17] The calculated TTT diagram shows two C curves, one for σ and the other for χ. The nose of the C curve for σ phase locates at a temperature close to 850°C and at a time of ~10 min while the nose for χ phase occurs towards to a lower temperature and a shorter time. The relative positioning of the C curves for σ and χ is quite

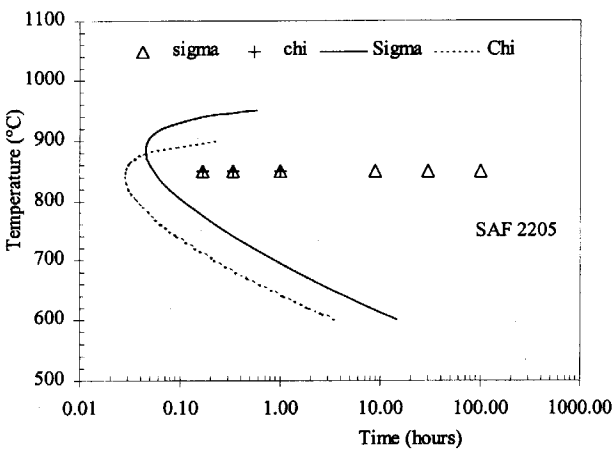

2 Calculated time–temperature transformation diagram for start of σ and χ phase formation in SAF 2205 duplex stainless steel: symbols represent experimental results from Thorvaldsson *et al.*[17]

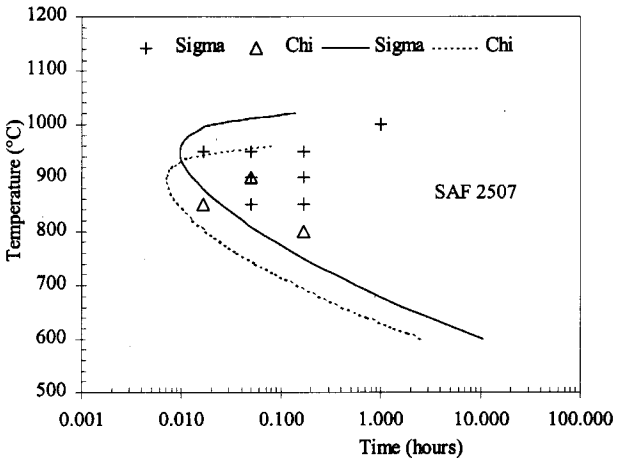

3 Calculated time–temperature transformation diagram for start of σ and χ phase formation in SAF 2507 super duplex stainless steel: symbols represent experimental results from Nilsson and Wilson[18]

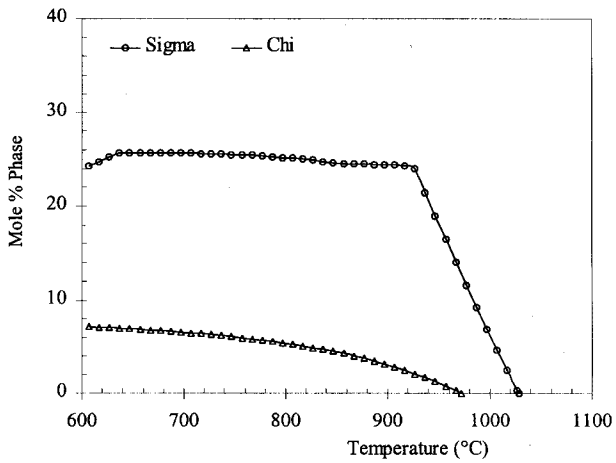

5 Calculated amount of σ and χ phase in SAF 2507 duplex stainless steel with the other phase suppressed

typical for DSS[2,18,21] and, in the case of SAF 2205, is evidenced by the fast formation of χ below the nose of the C curve of σ before it subsequently transforms to σ, which is the stable equilibrium phase. A similar type of TTT diagram is both calculated and experimentally observed for SAF 2507 (Fig. 3). Since SAF 2507 contains a higher lever of Cr and Mo, the nose times are shorter and towards higher temperatures compared with those in SAF 2205. It takes less than 1 min for the σ phase formation at around 900°C, which is consistent with the experimental observation.[18]

At first sight, the appearance of χ in SAF 2205 and SAF 2507 may appear strange because the equilibrium temperature range for χ formation is well below that of σ. Figure 1 shows the equilibrium phases formed in SAF 2205 while Fig. 4 shows a similar diagram for SAF 2507. However, when the formation of each phase is considered separately (Fig. 5), it can be seen that the metastable solvus for χ is very close to that of σ and it is this solvus that has to be considered when modelling the decomposition of the undercooled, supersaturated solid solution. The faster transformation kinetics for χ are modelled as being due to enhanced nucleation, as has been previously postulated,[22] with N_0 for χ taken as being about one order of magnitude larger than for σ.

As well as calculating the start of transformation, the approach adopted here also appears to successfully account for larger amounts of transformation. Figure 6 shows the calculated TTT diagram for the formation of 5 vol.-% of σ phase in Zeron 100, a super DSS, and compares this to experiment.[23,24] There is reasonable agreement between the calculated nose time and nose temperature and the experimental data, which are rather scattered.

Figure 7 shows the calculated TTT diagrams for two types of super duplex stainless weld metals with the basic compositions of Fe–25Cr–9Ni–(3–4)Mo–0·25N.[25] The WCuN alloy (Fig. 7*a*) contains about 0·9W and 0·6Cu while the SDN alloy (Fig. 7*b*) is virtually W and Cu free. Both TTT curves of σ and χ are calculated for the 1% intermetallic formation. The switch from σ formation to χ formation matches the experimentally observed bay area rather well. For 5% intermetallic formation, only the TTT curve for σ is plotted. This is based on the consideration that the amount of χ phase in super duplex stainless is usually very small (less than 2 vol.-% in Zeron 100 steels) and also due to the fact that it is a transient phase that will transform to σ.[21]

It is also of interest to model the transformation kinetics of the chromium rich α' phase. This phase forms between 300–500°C, with its peak transformation rate around 475°C, giving rise to what is often referred to as the 475°C embrittlement. The transformation occurs because the ferrite from the duplex treatment becomes unstable with respect to the formation of almost pure Cr. This instability is usually understood to arise from the Fe–Cr binary phase diagram

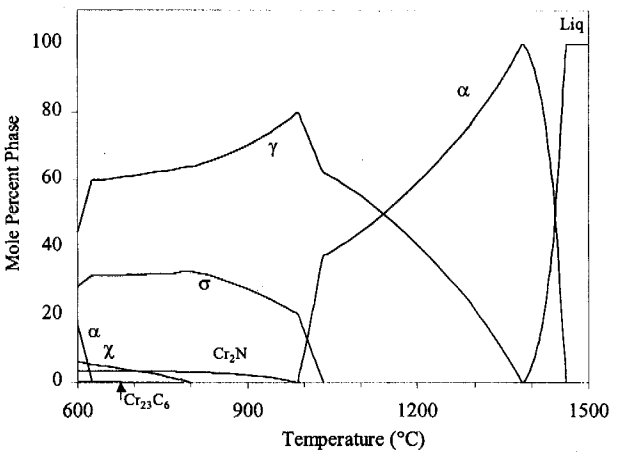

4 Calculated phase amount *v.* temperature plots for SAF 2507 alloy

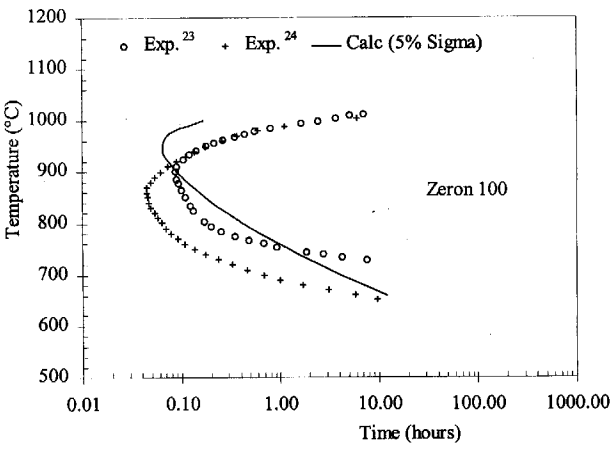

6 Calculated time–temperature transformation diagram for formation of 5 vol.-% σ phase in Zeron 100 steel: symbols represent digitised points of experimental curves from Prouhèze and Martin[23] and Wang *et al.*[24]

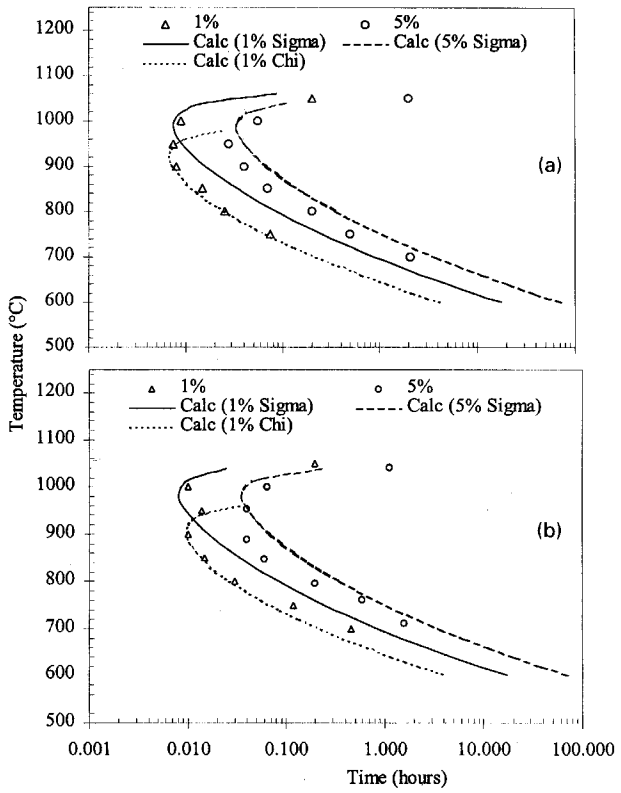

a weld metal WCuN; *b* weld metal SDN

7 Calculated time–temperature transformation diagrams for 1 vol.-% σ/χ phase and 5 vol.-% σ phase formation in two super duplex weld metals: symbols represent experimental results from Nilsson *et al.*[25]

where there is a miscibility gap in the α(Fe,Cr) solid solution. This causes the breakdown of the high temperature solid solution to αFe and αCr, with the latter alternatively described as α′. It is sometimes postulated that α′ may form by spinodal decomposition.[2] However, detailed thermodynamic analysis by Hayes *et al.*,[26] on Fe–Cr–Ni based alloys, shows that alloys with the Cr and Ni levels usually associated with DSS are unlikely to decompose by spinodal decomposition above 300°C. Instead, transformation is suggested to be by a nucleation and growth process, which is how the transformation has been treated in this paper. Figure 8 shows the comparison between a calculated TTT

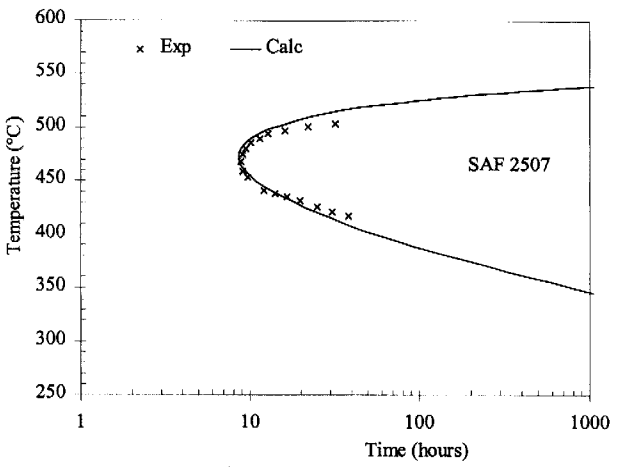

8 Calculated time–temperature transformation diagram for start of α′ phase formation in SAF 2507 alloy: symbols represent points of digitisation of experimental curves from Nilsson[2]

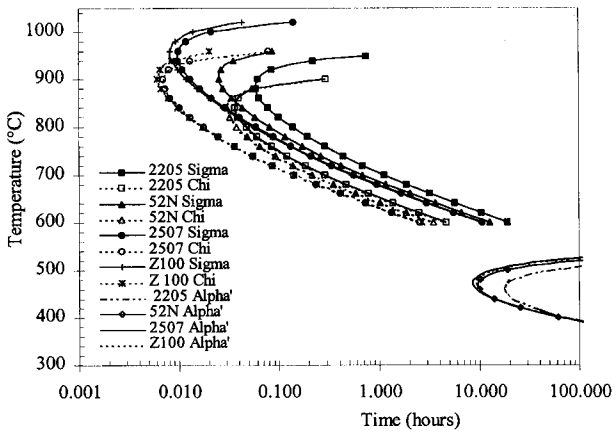

9 Calculated time–temperature transformation diagrams for σ, χ, and α' phase formation in duplex stainless steels

curve for α′ and that observed experimentally for SAF 2507.[2]

In order to demonstrate the effect of composition on the phase transformation behaviour, the TTT diagrams for σ, χ, and α' formation in different grades of duplex steels were calculated and summarised in Fig. 9. It is evident that adding Cr, Mo, and W will promote the formation of the intermetallic phases and, apart from UR 52N, the C curves for χ tend to lie towards lower temperatures and shorter times than for σ. This sequence of precipitation has been experimentally confirmed in these alloys.[17,18,21] However, the competition between σ and χ can change depending on the chemistry of the alloy. For example, it has been reported that χ phase is not present in a 29Cr–6Ni–2Mo–0·38N super DSS owing to its higher level of nitrogen and lower level of molybdenum.[27] The calculated nose temperatures for the α' formation for all the alloys are ~475°C, which correctly reflects the experimental situation. It has been noted that the nose time for α' formation in SAF 2205 is ~20 h, while the nose times in SAF 2507, Zeron 100 and UR 52N alloys are very close to a value of ~10 h. This may be due to the higher Cr content in the latter three alloys.

MECHANICAL PROPERTY OF SOLUTION HARDENED DUPLEX STAINLESS STEELS

Tensile and hardness calculations

The first step in calculating the proof stress is to obtain the composition and volume fraction of the austenite and ferrite in the solution treated condition. This is achieved by thermodynamic calculation. It should be noted that as the molar volumes of austenite and ferrite are very similar, the calculated mol.-% value provides a very reasonable estimate for the volume fraction. A typical result for a Zeron 100 duplex steel is given in Table 2. It can be seen that γ and α have roughly equal volume percentages at this temperature, but the γ phase is enriched in Ni, Cu, Mn, C, and N while the α phase is enriched in Cr, Mo, W, and Si.

In order to complete the calculation for DSS, the mechanical properties for both austenite and ferrite need to be calculated by using the model described before.[6] Figures 10 and 11 show a comparison between experimentally observed and calculated tensile property values for a wide range of multicomponent austenitic and ferritic stainless steels that form the basis for the mechanical property modelling undertaken in the present paper. Excellent agreement between calculated and observed values is obtained.[28,29]

Once the requisite properties of austenite and ferrite are obtained, the 0·2% proof stress of the duplex material can be calculated using equation (16). Figure 12 shows the

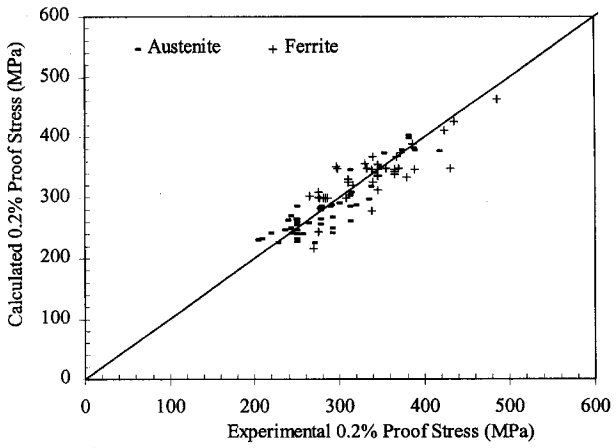

10 Calculated versus experimental 0·2% proof stress of various solution hardened austenitic and ferritic stainless steels: symbols represent experimental values from Pickering[28] and Hunt[29]

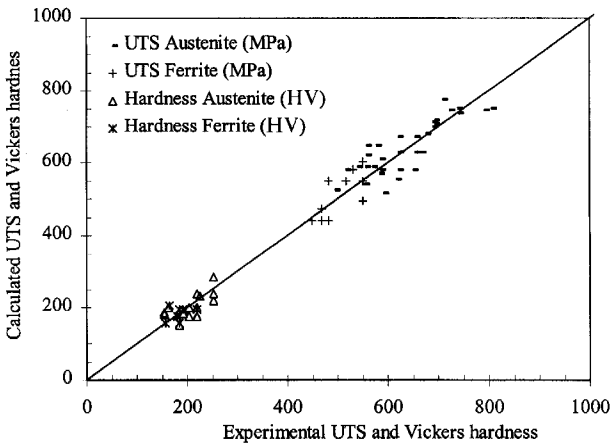

11 Correlation of experimental mechanical properties with values calculated from 0·2% proof stress for austenitic and ferritic stainless steels: symbols represent experimental values from Pickering[28] and Hunt[29]; Vickers hardness indentation geometrically similar regardless of load size

comparison between calculated and experimental 0·2% proof stress for various DSSs at room temperature. The observed results are from a variety of authors[1,30–32] and the compositions of the alloys vary from low alloyed materials to super DSS. Except for the alloys quoted by Gysel,[31] which are cast alloys with grain sizes of ~30 μm, the grain size for the other DSS is very small, in the region of 10 μm. The calculated results are in excellent agreement with experiment.

The phase fractions of austenite and ferrite in DSS exert a considerable effect on most properties of DSS and are mainly determined by composition and heat treatment.[33] Figure 13 illustrates the variation of 0·2% proof stress of a DSS as a function of the solution treatment temperatures with the assumption that they have the same grain sizes. The proof stress of austenite and ferrite phases is also included in this figure. It can be seen that the proof stress strength of the

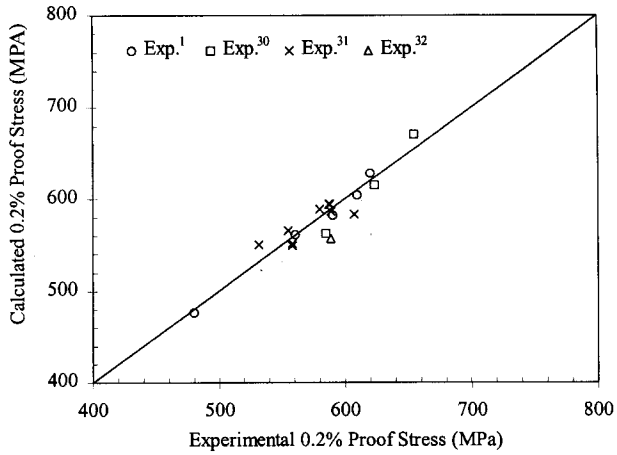

12 Comparison between calculated and experimental 0·2% proof stress of various solution hardened duplex stainless steels

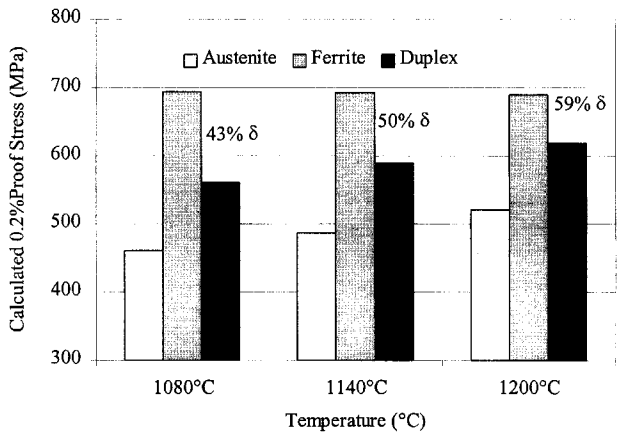

13 Calculated 0·2% proof stress for Zeron 100 alloy as function of solution treatment temperature: proof stress of corresponding austenite and ferrite phases also included

duplex alloy increases with increasing solution temperature owing to the higher volume fraction of ferrite, since the strength of ferrite at the appropriate grain size is higher than that of austenite. However, it has been reported that higher solution temperature treatment could result in a decrease in toughness.[33] To balance the strength, toughness and corrosion resistance, the optimum heat treatment temperature is to produce equal amount of austenite and ferrite.

As mentioned in the previous section, once the proof stress is calculated, the tensile strength and the hardness can be predicted via the inter-relationship among these properties. Figure 14 shows the agreement between calculated and experimental values, which is also very good.

Ductile/brittle fracture transition

Among the various types of precipitates, σ is the most important owing to its high volume fraction and much

Table 2 Calculated phase amount and concentration of alloying elements in austenite and ferrite at 1140°C for Zeron 100 alloy

Phase	Phase amount, mol.-%	Element concentration, wt-%									
		Fe	C	Si	Mn	Cr	Mo	Ni	Cu	N	W
γ	50·01	62·13	0·028	0·35	1·11	23·19	2·71	8·70	0·84	0·430	0·51
δ	49·99	60·76	0·002	0·45	0·89	26·82	4·29	5·29	0·56	0·049	0·89

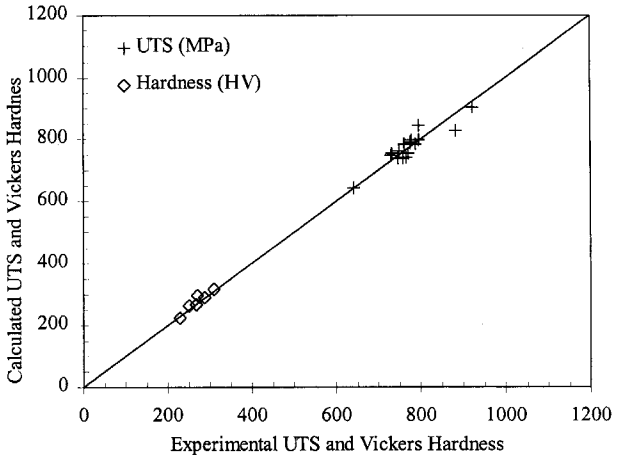

14 Correlation of experimental mechanical properties with values calculated from 0·2% proof stress for duplex stainless steels

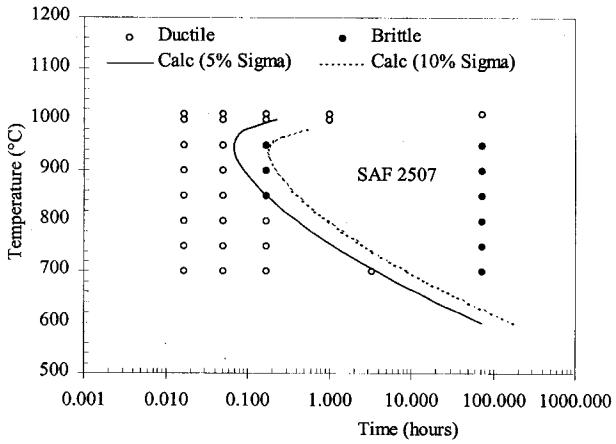

16 Calculated time–temperature transformation diagrams for 5 and 10 vol.-% of σ phase formation in SAF 2507 super duplex stainless steel: symbols refer to experimental results above and below 27 J, which is room temperature ductile to brittle transition value from Nilsson and Wilson[18]

experimental work has been done to show its effect on the mechanical properties.[1,17,33] The general conclusion is that the proof stress, tensile stress and hardness increase while the toughness decreases with increasing amount of the σ phase. However, while tensile strength, proof strength and hardness tests are relatively insensitive to small amounts of σ phase (<10 vol.-%), a Charpy test reveals a very sharp decrease of toughness at an early stage of phase transformation.

Figures 15 and 16 show, respectively, the correlation of the calculated TTT diagrams for 5 and 10 vol.-% of σ with the superimposed Charpy test data for SAF 2205 and SAF 2507.[17,18] The experimental curves roughly represent a critical impact energy of 27 Joules, which is the critical limit for conventional toughness accepted by DSS users. It is evident that the transition curves from ductile to brittle fracture lie within the TTT curves for 5 and 10 vol.-% of σ, which is consistent with the observed results.[18]

Conclusions

In this paper, models have been described for the calculation of time–temperature transformation (TTT) diagrams and mechanical properties of duplex stainless steel (DSS). The methodology is very flexible and there is no restriction on the number of components or phases taking part in the calculation, as long as the necessary thermodynamic and kinetic data are available. The approach can be used in a predictive fashion using only the alloy composition and duplexing temperature, the latter being obtained from a thermodynamic calculation. The main conclusions are summarised below.

1. The TTT diagrams for a variety of DSSs have been calculated and compared with experimental observation. The agreement in all cases is very good. An advantage of the current model is that few input parameters need to be empirically evaluated. Where empirical values are used, for example in consideration of shape and nucleant densities, specific values have been defined for each precipitate type (i.e. σ, χ, or α'). Consequently, once these values are defined they have been self-consistently applied to all types of DSSs and the model can therefore be used in a predictive fashion.
2. It has proved possible to model the faster transformation kinetics of the χ phase by considering that there are an increased number of nucleant sites available for this phase compared with σ. The model then correctly displays the observed characteristic of χ formation whereby the nose temperature lies at lower temperatures than for σ but at shorter times. It has also proved possible to model the formation of the metastable precipitate α' successfully.
3. A model that calculates solid solution strengthening of ferrite and austenite, as a function of composition and grain size has been used to calculate the proof stress of the austenite and ferrite phases in a duplex alloy. The resultant values have been combined using a simple mixture model to predict the proof stress of a variety of DSSs. Good agreement between calculated values and experimental observation is found.
4. Using previously established relationships, values for tensile stress and hardness have been calculated from the 0·2% proof stress and compared with experiment. The agreement is very good.
5. Time–temperature transformation calculations for SAF 2205 and SAF 2507 show that the ductile to brittle transition as revealed by Charpy test is associated with between 5 and 10 vol.-% of σ in good agreement with values suggested in the literature.

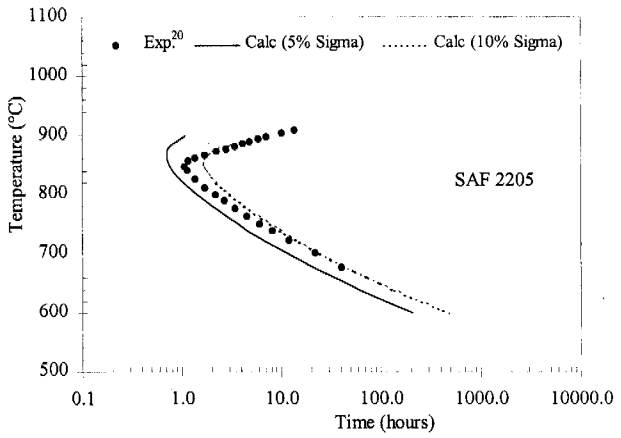

15 Calculated time–temperature transformation diagrams for 5 and 10 vol.-% of σ phase formation in SAF 2205 super duplex stainless steel: symbols represent experimental values for room temperature ductile to brittle transition from Thorvaldsson *et al.*[17]

References

1. J. CHARLES: in 'Duplex stainless steels 94', (ed. T. G. Gooch), paper K1; 1994, Glasgow, The Welding Institute.

2. J. O. NILSSON: *Mater. Sci. Technol.*, 1992, **8**, 685–700.
3. M. COURTNALL and F. B. PICKERING: *Met. Sci.*, 1976, **10**, 273–276.
4. K. J. IRVING, T. GLADMAN, and F. B. PICKERING: *J. Iron Steel Inst.*, 1969, **207**, 1017–1027.
5. H. NORDBERG: in 'Proceeding on innovation stainless steel', 217–229; 1993, Milan, Associazone Italiana di Metallurgia.
6. X. LI, A. P. MIODOWNIK, and N. SAUNDERS: *J. Phase Equilibria*, 2001, **22**, 247–253.
7. N. SAUNDERS, X. LI, A. P. MIODOWNIK, and J. PH. SCHILLE: Proc. Symp. on 'Materials design approaches and experiences', (ed. J.-L. Shao *et al.*), 185–197; 2001, Warrendale, PA, TMS.
8. N. SAUNDERS and A. P. MIODOWNIK: 'CALPHAD – calculation of phase diagrams', (ed. R. W. Cahn); 1998, Oxford, Elsevier Science.
9. U. R. KATTNER, W. J. BOETTINGER, and S. R. CORIELL: *Z. Metallkd*, 1996, **87**, 522–528.
10. D. A. PORTER and K. E. EASTERLING: 'Phase transformations in metals and alloys', 287–290; 1992, London, Chapman and Hall.
11. J. W. MARTIN, R. D. DOHERTY, and B. CANTOR: 'Stability of microstructure in metallic systems'; 1997, Cambridge, Cambridge University Press.
12. X. LI, N. SAUNDERS, and A. P. MIODOWNIK: Proc. Symp. on 'Materials design approaches and experiences', (ed. J.-L. Shao *et al.*); 2001, Warrendale, PA, TMS.
13. N. SAUNDERS and A. P. MIODOWNIK: *Mater. Sci. Technol.*, 1988, **4**, 768–777.
14. D. TURNBULL: *J. Appl. Phys.*, 1950, **21**, 1022–1028.
15. J. FRIDBERG, L. TÖRNDAHL, and M. HILLERT: *Jernkont. Ann.*, 1969, **153**, 263–276.
16. J. ASKILL: 'Tracer diffusion data for metals, alloys and simple oxides', Chapters 2–3; 1970, New York, NY, Plenum Press.
17. T. THORVALDSSON, H. ERIKSSON, J. KUIKA, and A. SALWEN: in 'Stainless steel 84', 101–105; 1985, London, The Institute of Metals.
18. J. O. NILSSON and A. WILSON: *Mater. Sci. Technol.*, 1993, **9**, 545–554.
19. E. O. HALL: 'Yield point phenomena in metals and alloys', 38–40; 1970, London, Macmillan.
20. Z. FAN, P. TSAKIROPOULOS, and A. P. MIODOWNIK: *J. Mater. Sci.*, 1994, **29**, 141–150.
21. X. LI: PhD thesis, University of Birmingham, UK, 1997.
22. H. L. CAO, S. HERTZMAN, and W. B. HUTCHINSON: in 'Stainless steel 87', 454–461; 1988, London, The Institute of Metals.
23. J. C. PROUHÈZE and G. MARTIN: in 'Duplex stainless steels 91', (ed. J. Charles and S. Bernhardsson), 632–637; 1991, Paris, Les Editions de Physique.
24. X. G. WANG, D. DUMORTIER, and Y. RIQUIER: in 'Duplex stainless steels 91', (ed. J. Charles and S. Bernhardsson), 127–134; 1991, Paris, Les Editions de Physique.
25. J. O. NILSSON, T. THUTALA, P. JONSSON, L. KARLSSON, and A. WILSON: *Metall. Trans. A*, 1996, **27A**, 2196–2208.
26. F. H. HAYES, M. G. HETHERINGTON, and R. D. LONGBOTTOM: *Mater. Sci. Technol.*, 1990, **6**, 263–272.
27. J. O. NILSSON, P. KANGAS, T. KARLSSON, and A. WILSON: *Metall. Trans. A*, 2000, **31A**, 35–45.
28. F. B. PICKERING: in 'The metallurgical evolution of stainless steels', (ed. F. B. Pickering), 1–42; 1979, London, ASM/TMS.
29. M. W. Hunt (ed.): 'Guide to engineered materials (GEM) – advanced materials & processes', Vol. 159, 51–66; 1999, Materials Park, OH, ASM International.
30. E. HÄMÄLÄINEN, A. LAITINEN, H. HÄNNINEN, and J. LIIMATAINEN: in 'Duplex stainless steels 94', (ed. T. G. Gooch), paper 122; 1994, Glasgow, The Welding Institute.
31. W. GYSEL and R. SCHENK: in 'Duplex stainless steels 91', (ed. J. Charles and S. Bernhardsson), 1331–1340; 1991, Paris, Les Editions de Physique.
32. H. LOUIS, H. J. KARKOSCH, and J. STRUVE: in 'Duplex stainless steels 91', (ed. J. Charles and S. Bernhardsson), 787–794; 1991, Paris, Les Editions de Physique.
33. C. V. ROSCOE, K. J. GRADWELL, and G. W. LORIMER: in 'Stainless steel 87', 563–577; 1988, London, The Institute of Metals.